Cep57 coordinates genome stability and cell cycle progression in early embryos

Sharada Iyer[1,2], Lakshmi Prasanna Sai Madamanchi[1], Advait Gokhale[1], Megha Kumar[1,2*]

[1]CSIR-Centre for Cellular and Molecular Biology (CSIR-CCMB), Habsiguda, Uppal road, Hyderabad-50007, India

[2]Academy of Scientific and Innovative Research (AcSIR), Ghaziabad-201002, India

[*]Correspondence:

Megha Kumar, Ph.D.

Senior Scientist

CSIR-CCMB, Habsiguda, Uppal Road, Hyderabad 500007

Telangana, India

Email: meghakumar.ccmb@csir.res.in, ORCID: 0000-0002-3842-9975

Abstract

Centrosome is a key cell signaling hub, orchestrating mitotic events and the distribution of cell fate determinants. Centrosomal dysfunction results in mitotic aberrations such as microtubule disorganization, mitotic spindle anomalies, and orientation defects, leading to cell division errors. Yet, how centrosomal defects are communicated to cell cycle checkpoints during embryogenesis remains unresolved. Centrosomal protein 57 (CEP57) is best known for its role in centrosome organization, where it regulates microtubule nucleation, stabilization, and spindle assembly. Here, we uncover previously undescribed, distinct functions of Cep57 in regulating G1/S progression, centrosome integrity, and DNA damage responses during early embryogenesis. In early zebrafish embryos, Cep57 localizes to both the nucleus and centrosomes, suggesting dual roles in cytoskeletal organization and nuclear cell cycle regulation. Cep57 interacts with Rad21, and its loss results in consequential depletion of Rad21, leading to supernumerary nuclei and defects in pericentriolar material organization. Our results also show that Cep57 interacts with Geminin, and it induces an Rb1-dependent G1 arrest. Hence, lack of Cep57 results in widespread cell cycle defects, genome instability, and increased apoptosis. Quantitative proteomics reveals induction of DNA damage responses and checkpoint pathways, indicating engagement of genome surveillance programs downstream of centrosome dysfunction. Thus, we show that Cep57 functions as a molecular bridge linking centrosome integrity to G1/S checkpoint control in early embryos. These cellular defects precede and likely underlie neural tissue apoptosis and microcephaly-associated characteristics observed in Cep57-deficient embryos. Together, our findings identify Cep57 as a critical integrator of centrosome organization, cell cycle progression, and genome stability, expanding its functional scope beyond canonical centrosome regulation during vertebrate embryogenesis.

Keywords:

Centrosome, Cep57, cell cycle, genome instability, apoptosis, microcephaly

Introduction:

Centrosomal protein 57 (CEP57) plays key roles in centriole dynamics, mitotic spindle formation, and organization. It is essential for pericentriolar matrix (PCM) organization, centriole duplication, and engagement. Lack of CEP57 results in PCM disorganization and precocious centriole disengagement, resulting in ectopic Microtubule Organizing Centres (MTOCs).[1–7] It also plays crucial roles in the nucleation and stabilization of microtubules and spindle formation, and its depletion results in misaligned chromosomes and multipolar spindles.[4,8,9,10] Further, it localizes to the kinetochores and interacts with microtubules to remove MAD1, and its abrogation results in impaired Spindle Assembly Checkpoint (SAC) signaling and chromosome segregation defects.[7,9,11] CEP57 also localizes to the cytokinetic midbody and aids in central spindle microtubule organization.[12] Mutations in the *CEP57* gene are associated with Mosaic Variegated Aneuploidy syndrome (MVA), an autosomal recessive disorder characterized by chromosome gain or loss in somatic cells, which results in mosaic aneuploidies. These patients exhibit microcephaly, skull deformities, facial dysmorphism, and predisposition to tumors. [1,6,13–15] The *Cep57* homozygous knockout was embryonic lethal, and the heterozygous mice exhibited severe vertebrate ossification defects and died shortly after birth. The murine cells showed aneuploidy, impaired centrosomal maturation, premature centriole disjunction, and chromosome segregation anomalies.[4,16] However, the mechanistic underpinnings of microcephaly mutations in *CEP57* remain unknown. Recent studies implicate the tight interplay of centrosomal pathways with DNA damage response to maintain genome integrity.[17] Yet, how centrosomal defects are communicated to cell cycle checkpoints during embryogenesis is poorly understood. Hence, understanding the contribution of centrosomal dysfunction to developmental disorders remains elusive.

Here, we investigate the developmental functions of *cep57* during vertebrate embryogenesis. We show that Cep57 localizes to the nucleus and spindle poles in the developing zebrafish blastulae, suggesting functions beyond its established centrosomal roles. The loss of Cep57 resulted in extensive DNA damage, micronuclei formation and mitotic errors. Mechanistically, we identify an interaction between Cep57 and cohesin member Rad21, which ensures faithful chromosome segregation and DNA damage response.

Further, we show that Cep57 deficiency also induces an Rb1-dependent G1 cell cycle arrest. Our experiments reveal a previously unrecognised regulatory interaction between Cep57 and an important G1/S checkpoint regulator, Geminin. Loss of Cep57 results in elevated levels of Geminin and, consequently, disruption of G1/S progression. Consistent with this model, comparative proteomic analysis identifies additional regulators of genome stability and cell cycle control that are altered upon Cep57 depletion. These include DNA damage–associated proteins such as Dapk1, Arid3b, Cpped1, and Pp2a, chromosome maintenance proteins like Smc4, Ctf8, along with cell cycle regulators including 14-3-3 proteins and Cdk7.

As CEP57 has been classically studied in centrosome-dependent mitotic events, and the associated MVA has been attributed to mitotic anomalies, our study expands its functional repertoire. In addition to its role in centrosome-associated mitotic errors, we identify Cep57 functions in G1/S progression and safeguarding genome stability during early embryogenesis. These cellular defects are coupled to neurodevelopmental anomalies, increased neural tissue apoptosis, reduced expression of neural crest specification genes, resulting in microcephaly-associated features. To summarize, we show that Cep57 depletion leads to checkpoint failure via Geminin and p53-p21-Rb1 signaling. Cep57 also plays vital role in genome survillence as loss of Cep57 functions result in defective DNA repair and mitotic errors during early development. Hence, *cep57*-associated microcephaly likely arises not only due to mitotic errors but also from defective G1/S cell cycle transition, genome instability and apoptotic loss of neural progenitors.

Results and Discussion:

Cep57 localizes to centrosomes and is essential for early neurodevelopment and maintenance of head size

To delineate developmental functions of *cep57*, we examined its expression and localization across developmental stages. During early embryonic development, Cep57 localizes to the spindle poles at metaphase (red asterisks, Fig. 1A, B) and in the nucleus in the zebrafish blastulae (white asterisk, Fig. S1A, Fig. 1B). As *cep57* was expressed ubiquitously during cleavage stages (256 cell stage), it is maternally inherited and continued to be expressed till the somitogenesis phase (Fig. S1B, S1D). The protein levels were also maintained across early

developmental stages till 1dpf (Fig. S1C). The spatio-temporal expression was restricted to the eye and brain during later phase of somitogenesis until 1dpf (red asterisk, Fig. S1D). To ascertain its developmental roles, we used a gene knockdown approach using antisense morpholinos (translation and splice blocker) against zebrafish *cep57* and its depletion was confirmed by immunoblotting with the morphant lysates (Fig. 1C).

The translation blocker morphants showed somitic defects (red asterisk, Fig. 1E), abnormalities in the brain architecture and organization, eye and otic vesicle defects (double red asterisks, Fig. 1E) along with a poorly developed anteroposterior axis (red arrow, Fig. 1E). We categorized the morphants as normal, like controls (P0), embryos with brain abnormalities (P1), embryos with brain abnormalities and anterior-posterior axis defects (P2), and the extremely severe phenotype with poorly developed brain and body axis (P3) (Fig. 1D, Fig. S2A). The severity of the phenotypes P0, P1, P2, and P3 increased in a morpholino concentration-dependent manner (Fig. S2B). To ascertain the specificity of the morpholinos, we performed rescue experiments by co-injecting the splice blocker morpholino and z*cep57* mRNA at 1-cell stage embryos and the co-injection of mRNA significantly rescued all the phenotypes (Fig. 1D, S2C). Thus, *cep57* is crucial for neurodevelopment and axis specification during early embryogenesis.

At later stages, the morphant larvae showed gross craniofacial defects, cardiac edema, and severe anteroposterior axis defects (Fig. S2D). The P1 and P2 morphants showed severe craniofacial dysmorphic features, cartilage, and skeletal abnormalities at larval stages (double red asterisk, Fig. 1F). The morphant larvae exhibited reduced head size and interpupillary distance (IPD) (Fig. 1G), indicative of a microcephaly-like phenotype. To confirm, we also examined the levels of microcephaly-associated genes *mcph1, wdr62, ankle2, map11, kif14*, and *aspm* (Fig. S3) and the morphants exhibited a marked reduction in all these genes (Fig. S3). The reduced expression of the microcephaly markers shows that *cep57* plays a key role in the maintenance of neural progenitor cell fate and regulating head size.

The craniofacial defects can be attributed to the reduced expression of neural crest specifier genes like *crestin* and *sox10*, as the craniofacial skeletal elements primarily develop from neural crest-derived mesenchyme.[18–20] *crestin* is a pan-neural crest marker, expressed in premigratory and migrating neural crest cells.[21] *snail2* and *sox10* are expressed in the premigratory cranial neural crest cells and are required for neural crest survival, specification, and migration.[20] As

expected, we observed severe down-regulation of *crestin*, *snail2*, and *sox10* in the *cep57* morphants at the early somitogenesis phase (red asterisk, Fig. S4A, B, C) and 24hpf P2 morphants (double red asterisk, Fig. S4D, E, F). The down-regulation of these specifier genes strongly suggests that *cep57* is essential to maintain the neural crest progenitor fate. Further, *sox2* is essential for the proliferation and maintenance of neural progenitors.[20,22,23,24] The morphants showed a severe downregulation of *sox2* (red asterisk, Fig. S4G), suggesting loss of neural progenitor cells and notochordal defects marked by *tbxta* expression in the *cep57* morphants (red arrow, Fig. S4H). Hence, gene expression analysis highlights the role of *cep57* in cranial neural crest specification and mesoderm patterning.

Cep57 is essential for cell survival and cell cycle progression

To further probe the cellular basis of microcephaly-like phenotype, we examined the extent of cell death in *cep57* morphants. Though the morphants showed embryo-wide apoptosis, particularly in the head, as shown by acridine orange staining (red asterisks, Fig. 2A) and fluorescein-based terminal deoxynucleotidyl transferase dUTP nick end labelling (TUNEL) staining (red asterisks, Fig. 2B). We next examined the morphants for cell cycle progression (Fig. 2C-F). Fluorescence-based flow cytometry analysis revealed a significant increase in the G1 phase and concomitant reduction in the G2/M phase, while the S phase remained unchanged in the 1dpf *cep57* morphants as compared to control (Fig. 2C, E). The *cep57* morphants showed reduced PH3 staining, indicating a reduction in M-phase cells (Fig. S5C). As development proceeds in time by 2dpf, the accumulation of cells in G1 phase resulted in a consequent reduction in the S phase, showing impaired G1/S transition (Fig. 2D, 2F). Thus, Cep57 plays a critical role in cell survival and cell cycle progression.

Loss of Cep57 results in PCM disorganization, genome instability, and supernumerary micronuclei

The whole embryo DNA content flow cytometry assay was validated by immunoblotting for cell cycle markers, Geminin and Cdk1 across developmental stages (Fig. 3A). Geminin is one of the master regulators of cell cycle progression, accumulating in S, G2, and M phases.[25] At G1,

Geminin levels are low and during G1-S transition, and high levels of Geminin in the G2 and M phase ensure that DNA re-replication is inhibited. At metaphase-anaphase transition, Geminin is degraded to prepare the cell for the next cycle. [26,27] Ectopic expression of Geminin in G1 elicits cell cycle arrest, failure to progress into S phase, and apoptosis. [28] The progression throughout the cell cycle also requires the regulatory oscillatory activity of cyclins and cyclin-dependent kinases (Cdks). Cyclin-dependent kinase 1 (Cdk1) regulates G1 to S and G2 to M phases, and its activity is modulated by phosphorylation and binding to Cyclin B1.[29] Cdk1 levels are low in G1, and activity increases by late G1 until anaphase.

During cleavage (64-128 cell stage), Geminin levels are unchanged in the *cep57* morphants (Fig. 3A). We observed a reduction of Cdk1 levels, corroborating with the flow cytometry analysis of reduced G2/M entry upon Cep57 depletion (Fig. 3A). However, Geminin levels increased as development proceeds in time, particularly in the sphere stage, gastrulation (50% epiboly) until 1dpf, suggesting that Cep57 depletion resulted in G1 arrest (Fig. 3A). The Cdk1 levels remain unchanged in the sphere stage in *cep57* morphants (Fig. 3A). Surprisingly, we observed an accumulation of Cdk1 during gastrulation upto 1dpf (Fig. 3A). Hence, we probed for inhibitory form of Cdk1, phospho Cdk1 (Tyr15) and observed a concomitant increase in the inhibitory form, suggesting that Cdk1 is maintained in the inhibitory state, strongly indicating inhibition of cell cycle progression and G1 arrest (Fig. 3A). The G1 arrest was further confirmed by increased levels of Cyclin E, DNA damage-induced G1 to S kinase (Fig. S5D).

To dissect the cause of reduced G2/M entry upon Cep57 depletion and as it localizes to the centrosomes in zebrafish blastulae, we investigated its role in centrosomal and mitotic progression. We thus examined the morphants for mitotic aberrations during early embryonic divisions (Fig. 3B). The morphants showed spindle pole focusing and pericentriolar matrix defects (red asterisks, Fig.3B, C, D), highlighting the centrosomal function of *cep57* in maintaining spindle pole integrity, in a manner akin to the *Xenopus* egg extract system.[7] However, the centriolar organization remained unperturbed upon Cep57 depletion (Fig. 3E). Further, aberrations in spindle pole focusing can result in the unequal distribution of chromosomes, genomic instability, and cell death.[30] Intriguingly, we observed the presence of supernumerary micronuclei, strongly indicating chromosome segregation defects, aneuploidy, and genomic instability (white asterisks, Fig. 3F). Collectively, these experiments suggest that

Cep57 depletion results in genome instability during early embryogenesis, thereby leading to impaired G1/S transition.

In order to further quantify genomic instability and DNA damage in *cep57* morphants, we performed the comet assay (Fig. 4A). The broken DNA fragments formed a typical "tail" in the morphant samples, showing that Cep57 depletion results in single/ double-stranded DNA break and formation of alkali-labile sites (Fig. 4A). In addition, we also used a random amplified polymorphic DNA (RAPD) PCR assay to check for genomic instability, DNA alterations, damage, and mutations. [31,32] The morphants showed variation in band intensity as well as loss of polymorphic bands in the amplification patterns with respect to the control (red arrows, Fig. S5A), corroborating a 38.7% reduction in genomic template stability (GTS%) (Fig. S5B). [31,32] Rad21, is a core cohesin complex member that enables the separation of sister chromatids and also mediates DNA damage response. The depletion of Rad21 results in impaired DNA damage response and is critical for repair. In addition to proteolytic cleavage during mitosis, it is also cleaved during nuclear fragmentation in apoptosis.[33,34] To ascertain the basis of genome instability, we checked Rad21 levels in the morphants and observed the depletion of Rad21 protein, indicating abrogation of DNA damage response upon Cep57 depletion (Fig. 4B). To investigate its role in DNA damage repair, we performed endogenous immunoprecipitation assays to identify Cep57 mediated DNA damage repair machinery. Our endogenous immunoprecipitation experiments revealed that Cep57 interacts with Rad21 (Fig. 4C), suggesting that Cep57-Rad21 interaction is essential for faithful chromosome segregation and functioning of the DNA damage repair machinery. The loss of Cep57 results in the abrogation of Rad21 and the cohesion complex, resulting in chromosome segregation errors, formation of extranuclear bodies or micronuclei coupled with extensive DNA damage.

Cep57 interacts with Geminin to regulate Rb1-mediated G1/S transition

DNA damage also induces the activation of the cell cycle checkpoint regulatory pathway involving p53-p21-Retinoblastoma 1 (Rb1) signaling. DNA damage causes p53 activation, which in turn induces *p21* expression. The high levels of p21 result in the Rb-E2F complex formation, downregulation of cell cycle genes, and finally leading to cell cycle arrest.[35] The *cep57* morphants showing DNA damage, also showed increased *p53* expression and

consequently, high levels of *p21* expression (Fig. 4D). To determine the mechanism by which *cep57* depletion results in G1 arrest, we examined the levels of G1/S checkpoint regulator Rb1, which, in active or hypophosphorylated form, binds to E2F transcription factor, represses target genes, preventing cells from entering S phase and propagation of damaged DNA.[36] Upon G1/S transition, when phosphorylated by CDKs, it releases E2F, resulting in cells to progress into S phase. The morphants showed reduced levels of phospho form of Rb1 (Ser 807/811), indicating that Rb1 is maintained in inactive state upon Cep57 depletion and hence resulting in inhibition of G1 to S transition (Fig. 4E). Next, we used Rb1 mutant zebrafish embryos to confirm if Cep57 induced G1 arrest is mediated by Rb1. Intriguingly, the increase in G1 phase and decrease in G2/M phase upon Cep57 depletion were rescued significantly in the Rb1 mutant background (Fig. 4F). Further, Geminin levels were also restored in the Cep57-depleted Rb1 mutant background (Fig. 4G). We then performed an endogenous immunoprecipitation assay to determine if Cep57 interacts with these G1/S checkpoint regulators. Interestingly, our immunoprecipitation results show that Cep57 interacts with Geminin, highlighting the mechanistic regulation of Cep57-mediated cell cycle progression (Fig. 4H). In support of this result, the overexpression of Cep57 mRNA restored the Geminin levels in the Cep57-depleted embryos, allowing normal cell cycle progression (Fig. 4I). These findings collectively show that Cep57 through its interaction with Geminin, helps to regulate its levels to promote cell cycle progression and and the loss of Cep57 results in an Rb1-mediated G1 arrest in the developing embryos.

To probe further into the mechanistic basis of the *cep57* knockdown phenotypes, we performed label-free LC-MS/MS proteomics analysis to identify differentially regulated proteins in *cep57* morphants (Fig. 5A). We confidently identified 121 upregulated and 65 downregulated proteins in the *cep57* morphants (Fig. S9). Owing to the limited mapping of the zebrafish proteome in multiple databases such as Panther, String, and ShinyGo, a total of 19 GO terms were identified, including biological processes for the upregulated category and a total of 18 GO terms, including molecular function for the downregulated proteins (Fig. S6). The GO terms of the fold-enriched biological processes were apoptosis, microtubule dynamics, vesicular trafficking, and cytoskeletal organization in the upregulated protein category (Fig. S6). For downregulated proteins, the GO terms for fold-enriched biological processes were chromosome condensation, sister chromatid cohesion, and segregation coupled with cell cycle regulators (Fig. S6). Hence,

gene ontology analysis corroborates our results to show that *cep57* depletion results in chromatid-associated defects and increased apoptosis-promoting factors, resulting in impaired cell cycle progression and a surge of apoptosis.

The comparative proteome analysis showed many interesting leads into Cep57 molecular functions. Consistent with our experiments showing DNA damage and increased apoptosis upon *cep57* depletion, the comparative proteome also revealed upregulation of pro-apoptotic proteins such as Arid3B, Cpped1, Protein phosphatase 2A (Pp2A), and Death-associated protein Kinase 1 (Dapk1) (Fig.5A, B). We also observed a corresponding upregulation of *dapk1* and *arid3b* transcripts in the morphants (Fig. 5B). ARID3B activates pro-apoptotic p53 target genes and induces apoptosis.[37] The overexpression of CPPED1 results in impaired cell cycle progression and promotes apoptosis.[38] PP2A upregulation leads to caspase 3 activation and hence has a pro-apoptotic function.[39] DAPK1 is a key regulator of cell death and mediates caspase-dependent and caspase-independent pro-apoptotic signaling. Recent reports also show its function in tumor suppression and neuronal cell death.[40–42] Thus, proteome profiling strongly suggests that Cep57 is essential for cell survival during early embryogenesis.

In cycling cells, normal cell cycle progression is critical for genome stability and integrity. The cell cycle checkpoints at G1/S, G2/M, and M/G1 ensure that each phase is completed without errors. 14-3-3 Proteins function at G1/S transitions and regulate the timing of mitosis. They interact with the CDK inhibitor p27, which mediates G1 arrest. In G1-arrested cells, depletion of 14-3-3 results in cell death.[43,44] The *cep57* morphants exhibiting DNA damage and G1 arrest showed downregulation of 14-3-3 protein (Fig. S9), indicating mitotic catastrophe and, hence, apoptosis. CTF8 is essential for the establishment of sister chromatid cohesion, and its depletion results in cohesion defects, chromosome segregation defects, and cell cycle arrest.[45,46] Our proteome data showed downregulation of Ctf8, indicative of impaired cell cycle progression and cell death (Fig. 5A, B). We also observed decreased Smc4 levels in *cep57* morphants (Fig. 5B). SMC4 is part of the condensin complex, and its phosphorylation induces G1 arrest and plays a key role in single-strand DNA break repair.[47–49] The downregulation of Ctf8 and Smc4 further reinforce our Cep57-Rad21 mediated genome survellience function. The comparative proteome data also showed a downregulation of Cyclin-dependent kinase 7 (Cdk7) in *cep57* morphant embryos (Fig. 5A). CDK7 phosphorylates CDK4 and CDK6 to initiate G1 progression and

CDK2 for G1/S transition. The G2/M transition is also induced by CDK7-mediated phosphorylation of CDK1. Mice lacking CDK7 showed increased apoptosis, and it is essential for neural progenitor proliferation.[50] CDK7 depletion results in decreased phosphorylation of CDK1 and CDK2, resulting in G1/S arrest. CDK7 inhibition also results in BAK and caspase 3/8 activation. It also upregulates ANNEXINV in the G1 phase, promoting apoptosis. [51–53] In summary, quantitative mass spectrometry-based proteome profiling of control and *cep57* morphants revealed a differential proteome of apoptosis-associated proteins, chromosome maintenance fators and cell cycle progression which provide fresh mechanistic insights into *cep57*-mediated cellular functions.

Conclusions:

CEP57 has classically been recognized for its pivotal role in centrosomal functions and mitotic events such as centriole biogenesis, organization of microtubule-based bipolar spindle, and faithful chromosomal segregation. Clinically, mutations in the *CEP57* gene have been linked to MVA, primarily characterized by microcephaly. At the cellular level, microcephaly is often associated with aberrations in centrosomal function, genome instability, and aneuploidy. The development of microcephaly is attributed to the failure of self-renewal or accumulated DNA damage in neural progenitor cells owing to checkpoint defects, DNA repair deficiencies, mitotic errors, and increased apoptosis. These findings underscore the importance of the interplay between the DNA damage response and centrosomal pathways in understanding the basis of microcephaly. Notably, several genes implicated in microcephaly, such as *MCPH1* and *CEP152*, possess dual roles in both DNA damage response and centrosomal function.[54]

In this study, we probe the developmental functions of *cep57* and we demonstrate that it localizes to centrosomes and the nucleus during early embryogenesis. Loss of Cep57 resulted in extensive DNA damage and formation of micronuclei, and the Cep57-Rad21 interaction is crucial for acurate chromosome segregation and functioning of the DNA damage repair mechanisms. Further, Cep57-mediated DNA damage also resulted in an Rb1-mediated G1 arrest in the embryos. At the molecular level, Cep57 interacts with Geminin and its depletion leads to elevated levels of Geminin, ultimately resulting in abrogation of G1/S transition. The

comparative proteome analysis also highlights differential expression of other molecular regulators of cell cycle progression, chromosome maintenance and activation of DNA damage inducing proteins. As the functions of CEP57 have largely been centrosomal, often associated with mitotic events, the MVA-associated phenotypes were attributed to these mitotic aberrations. While our findings corroborate the centrosomal mitotic anomalies, we also highlight a significant contribution of disrupted G1/S transition and DNA damage to the observed phenotypes. Specifically, we identify novel functions of *cep57* in cell cycle progression, maintenance of spindle pole integrity, faithful chromosome segregation, and genome stability during vertebrate embryogenesis. The loss of Cep57 resulted in neurodevelopmental defects, increased apoptosis in the neural progenitors, decreased expression of neural crest specifier genes, and microcephaly-associated features. These findings suggest that the microcephaly phenotypes associated with *cep57* deficiency may result not only from mitotic defects but also from impaired progression through the G1 phase of cell cycle, genome instability, and increased apoptosis (Fig. 5C).

In summary, this study uncovers novel, multifaceted roles of *cep57* during embryogenesis. While we provide strong evidence that Cep57 is a key regulator of G1/S cell cycle progression, we cannot entirely rule out the functional redundancy with other Cep family members, particularly regarding its mitotic roles, as we have investigated the cellular and developmental functions in an *in vivo* animal model-based knockdown system. Furthermore, although our proteomic analysis yielded a limited set of candidate proteins, likely due to incomplete mapping of the zebrafish proteome in public databases, it nevertheless identified several critical proteins involved in chromosome organization, cell cycle regulation, and apoptosis. In conclusion, the *cep57*-deficient microcephaly model provides a valuable system for dissecting the molecular mechanisms underlying the MVA-associated microcephaly. Our findings open new avenues for investigating broader roles of *cep57* functions in other cell cycle checkpoints, apoptotic regulation, and maintenance of chromosome integrity, which will be crucial to uncover its diverse cellular functions.

Methods:

Zebrafish lines, MO injection, and characterization of phenotypes

Tubingen strain (TU-AB) zebrafish were raised according to standard protocols as described earlier. Retinoblastoma (RB1) mutant lines were kindly provided by Dr. Indumathi Mariappan, BRIC inSTEM, Bangalore, India (ZFIN ID: ZDB-ALT-250929-16). All experiments were performed according to protocols approved by the Institutional Animal Ethics Committee of the Council of Scientific and Industrial Research, Centre for Cellular and Molecular Biology, India. Embryos were obtained from the natural spawning of adult fish, kept at 28.5°C, and staged according to hours after fertilization. [55] The endogenous *cep57* levels were depleted by using MO *cep57* translation blocker, 5'- AGGCTTTTGAGTTCGTCTCCATTAA-3′ and cep57 splice blocker, 5'-TGTCATAATGGACTCACAAGCTCAT-3' (Gene Tools). For rescue experiments, cep57 mRNA was *in vitro* transcribed (AM1340, Thermo Scientific), and 50pg of mRNA was co-injected along with c*ep57* splice MO in each embryo at the one-cell stage. The embryos were then analyzed for gross morphological defects and survival at later stages of development (till 5dpf) and were imaged in Zeiss Stemi508 stereomicroscope.

RNA isolation and Quantitative PCR

Total RNA was isolated from 100 embryos for each group using the RNA isolation kit (MN; 740955.50) as per the manufacturer's protocol. cDNA was prepared using the PrimeScript 1st strand cDNA synthesis kit (TaKaRa; 6110A). Quantitative real-time PCR (qPCR) was setup in ViiA7 Real-Time PCR System (Applied Biosystems) using the prepared cDNA as a template along with PowerSYBR Green PCR master mix (Applied Biosystems, cat. no. 4367659). The following program was used: 40 cycles of 95 ^{0}C -10min., 95 ^{0}C -15 sec., 60 ^{0}C -1 min., 95 ^{0}C -15 sec., 60 ^{0}C -1 min., 95 ^{0}C -15 sec. Zebrafish *β-actin* was used as an internal control. The gene expression levels were measured in triplicates for control and morphants. The fold change of the genes tested was calculated using the $2^{-\Delta\Delta Ct}$ (the delta-delta-Ct) method. All primers used in this study are listed in Fig.S8.

Antisense riboprobe preparation

For cloning sequence-specific exonic fragments to synthesize riboprobes, total RNA was isolated from a pool of 100 embryos (24hpf) of the TU-AB strain using an RNA isolation kit (MN; 740955.50). The total RNA was used to prepare cDNA using the PrimeScript 1st strand cDNA synthesis kit (TaKaRa, Cat. # 6110A). Sequence-specific primers were used to amplify the specific gene fragment and cloned into the pGEMT easy vector, and the sequence was verified. The sequence-verified plasmid was linearised using Nco1, and antisense digoxigenin (DIG)-labeled riboprobes were synthesized using the DIG RNA labeling kit (Roche #11175025910). [20]

Whole Mount RNA in Situ Hybridization

The control and the morphant embryos of the desired developmental stage were dechorinated and fixed in 4% paraformaldehyde (PFA) in PBS overnight. The embryos were then washed with PBT (1× PBS and 0.1% Tween 20) and stored in methanol at -20 ^{0}C overnight. Embryos were rehydrated using decreasing gradation of Methanol-PBT followed by pre-warmed hybridization wash buffer (50% formamide, 1.3 × SSC, 5 mM EDTA, 0.2%, Tween-20) and blocking in pre-warmed hybridization mix buffer (50% formamide, 1.3 × SSC, 5 mM EDTA, 0.2%, Tween-20, 50 µg/mL yeast t RNA, 100 µg/mL heparin) for 5 hours at 55 ^{0}C. DIG labelled RNA probe was added (1ng/ul) and kept overnight at 55 ^{0}C. The next day the embryos were washed with a prewarmed hybridization mix buffer followed by washes of gradation of 2X SSC (20X SSC stock-3M NaCl, 0.3M sodium citrate, pH7.2), Hybridization wash buffer, 0.2XSSC and TBST (0.5 M NaCl, 0.1 M KCl, 0.1 M Tris, pH 7.5 and 0.1% Tween 20) at room temperature. The embryos were then given a TBST wash and then blocked in 10% heat inactivated fetal bovine serum (Gibco; 16210-064) in TBST for 3 hours at room temperature. Anti-DIG antibody (1:5000) was added and incubated overnight at 4°C. Next day, four washes of TBST were given at room temperature followed by four washes of NTMT (0.1M NaCl, 0.1 M Tris-Cl at pH 9.5, 0.05M MgCl2, 1% Tween-20) and stained with 1-step NBT/BCIP solution (Thermo scientific, cat. no. 34042). Fresh NTMT was added to stop the reaction for both control and morphant embryos simultaneously and photographed using Zeiss Stemi508 stereomicroscope and Zeiss AxioZoom V16 microscope.[20]

Western Blot analysis

Lysates of embryos younger than 1dpf were prepared by homogenizing approximately 100 embryos using RIPA buffer (20mM Tris–HCl, pH 7.4; 150mM NaCl; 5mM EDTA; 1% NP-40; 0.4% sodium deoxycholate, 0.1% SDS and 1× Protease inhibitor cocktail). The lysis was carried by incubating on ice for 15 minutes with intermittent vortexing. The homogenized lysates were centrifuged (12000 rpm for 20 min at 4°C), and supernatants were collected. The samples were then boiled in Laemmli buffer at 95^0C for 10 mins. For 1dpf embryos, the embryos were first dechorinated and then deyolked by gentle pipetting using deyolking buffer (55mM NaCl, 1.8mM KCl, 1.25mM $NaHCO_3$) followed by centrifugation at 3000rpm for 30secs. The embryos were then washed using wash buffer (110mM NaCl, 3.5mM KCl, 2.7mM $CaCl_2$, 10mM Tris HCl, pH8.5), centrifuged at low speed, and the supernatant was discarded. The pellet was then boiled in Laemmli buffer at 95^0C for 10 mins. 20 µg of total protein was loaded in each lane and run on a 10% SDS-PAGE gel using Tris-Glycine SDS buffer for the detection of endogenous proteins. Proteins were then transferred to methanol-activated PVDF membranes (Merck Millipore, ISEQ00010) by electro-blotting. The membranes were then blocked either in 5% non-fat dry milk (sc-2324) or 5% BSA (Bovine serum albumin, for phosphoproteins) prepared in TBST (20 mM Tris HCl, pH 7.5, 150 mM NaCl, 0.05% Tween 20) for 1 hour. The blots were probed with primary antibody prepared in 1% blocking solution for 14-16 hours at 4^0C. The blots were then washed with 1X TBST three times and incubated with HRP-conjugated secondary antibody for 1 hr. The blots were then washed again three times with TBST and developed for chemiluminescence signal using the chemiluminescent substrate (Thermo scientific- 34577) and captured in the Vilber-Lourmat Chemiluminescence System. The primary and secondary antibodies used in this study are listed in Fig.S7.

Nuclear cytoplasmic fractionation

Ice-cold 0.1% NP40 prepared in PBS was added to 200 dechorinated and deyolked, wild-type embryos and gently pipetted 5-10 times. 200 µL of lysate was collected as the whole embryonic lysate. The remaining sample was centrifuged at 2000 rpm for 5 minutes. The supernatant was carefully collected as the cytoplasmic fraction. To the pellet, ice-cold 0.1% NP0/PBS was added, and gentle pipetting was done. The sample was again centrifuged, and the supernatant was discarded. The pellet contains the nuclear fraction. 2X Laemmli buffer was added to all the three

fractions, properly lysed, and heated at 95 °C for 10 mins. The purity of the fractions were confirmed by immunoblotting, probing with GAPDH (cytoplasmic marker) and LAMIN B1 (nuclear marker)[56]

FACS-based whole embryo cell cycle analysis

Embryos at the desired developmental stage were fixed in 4% PFA/PBS and subsequently dechorionated and deyolked. To obtain a single cell suspension, PBS was added to the embryos and disintegrated using a 24-gauge syringe. The cell suspension was then centrifuged at 1000 rpm for 2 mins at 4 ºC. The supernatant was collected in a fresh Eppendorf tube and centrifuged at 3000 rpm for 15 mins at 4 ºC. The pellet was resuspended in DAPI (10 µg /mL) prepared in PBS. The single cell suspension was then centrifuged at 3000 rpm for 15 mins at 4 ºC, resuspended in PBS, and analysed by flow cytometry. Cell cycle analysis was performed using Beckman Coulter Gallios flow cytometer and a total of 300000 singlet events were acquired for each group. The data was analysed using Kaluza Analysis 2.2 software, and plots were obtained with the histogram of the linear DAPI area using the J.V. Watson algorithm.

Acridine orange staining

Acridine orange (AO) staining was performed to detect the apoptotic cells in 1dpf embryos. The control and morphant embryos were dechorinated, stained with 5mg/L AO for 1 hour in the dark, and then washed with embryo water. The embryos were anesthetized with tricaine, and the bright green dots in the embryos indicated apoptotic cells. The number of apoptotic cells in the head region was counted using Image J software. The apoptotic cells in the embryos were photographed by Zeiss AxioZoom V16 microscope.[20,57]

TUNEL assay (terminal deoxynucleotidyl transferase dUTP nick end labelling)

Apoptotic cell death was assessed using the In Situ Cell Death Detection Kit, Fluorescein (Roche; 11 684 795 910), according to the manufacturer's protocol with slight modifications. Manually dechorionated 1dpf control and morphant embryos were fixed in 4% PFA in PBS overnight at 4 ºC, followed by methanol fixation for 48 hours. The embryos were then rehydrated using 50% methanol/PBS and washed thoroughly with PBS. Permeabilization was performed on ice for 15 min using 0.1% Triton X-100 in 0.1% sodium citrate and the embryos were incubated

in the TUNEL reaction mixture containing 5 µL enzyme solution and 45 µL label solution for 2 hours 30 minutes at 37 ºC in dark. The reaction was stopped by PBS washes and images were acquired using the Zeiss AxioZoom V16 microscope. Green fluorescent nuclei were considered TUNEL-positive, indicating DNA strand breaks in apoptotic cells.

Genomic DNA isolation and RAPD PCR

Genomic DNA isolation was done for both control and morphant embryos using the Macherey-Nagel nucleospin tissue kit as per the manufacturer's protocol. PCR reaction was set up using primer with sequence 5'-CCCGTCAGCA-3' and the isolated DNA(200ng) as a template for 25cycles. The PCR products were run on 2% agarose gel and visualized under UV light. The difference in the PCR profiles of control and morphants forms the basis of the genomic template stability (GTS). GTS= (1-a/n)*100, where a is the number of polymorphic bands in morphants and n is the total number of bands in control. GTS is expressed as a percentage with control set to 100%. [32]

Comet assay (single cell gel electrophoresis)

Microscopic slides were pre-coated with 1% agarose by spreading a thin, uniform layer over the slide surface and allowed to solidify overnight at room temperature. 20 µL single cell suspension was mixed with 30 µL 0.8% low-melting agarose and carefully spread onto the agarose-coated slides. The suspension was covered with coverslips and allowed to solidify at room temperature. The cells were lysed in freshly prepared lysis buffer (2.5 M NaCl, 100 mM EDTA, 10 mM Tris-Cl pH-9.5, 1% Triton X-100, 10% DMSO) at 4 °C for 90 mins, followed by incubation in electrophoresis buffer (300 mM NaOH in 1mM EDTA) for 30 mins. Electrophoresis was carried out at 15 V and 400 mA for 15–20 mins at 4 °C. Subsequently, slides were neutralized with 0.1 M Tris-HCl (pH 7.5) for 15 mins (three washes), fixed in 100% methanol for 5 min, and rehydrated in Milli-Q water for 10 mins. DNA was stained with SYBR Green (1:50) for 10 mins in dark, washed with Milli-Q water, and visualized in the Zeiss AxioZoom V16 microscope. To assess DNA damage based on comet tail formation, the acquired images were quantified using ImageJ software. Comet tail length was measured for 200 individual nuclei over three biological experiments by tracing the extent of DNA migration from the head to the end of the tail. The

mean tail length of morphant samples was compared to that of the corresponding control group, with increased tail length in morphants indicating elevated levels of DNA damage.

Skeletal preparations - Alcian blue and Alizarin red staining

Five day-old control and morphants larvae were fixed in 4% PFA/PBS overnight at 4^0C. The embryos were washed with 1XPBS and stored in methanol at -20 ^{0}C overnight. The staining solutions needed for bone and cartilage staining were prepared: Solution A (0.04% Alcian blue, 125mM MgCl2, 70% ethanol) and Solution B (1.5% Alizarin Red S). 1 ml of solution A and 20ul of solution B were added to the larvae and kept overnight at room temperature in dark with constant rocking. The staining solution was removed, and the larvae were washed twice with water. Then, embryos were then transferred to bleach solution (1% KOH, 1.5% H_2O_2) for 1 hour at room temperature followed by a gradation of Glycerol-KOH washes. The embryos were then stored in 50% glycerol-0.25% KOH, and the larvae were imaged using Zeiss AxioZoom V16 microscope. For microcephaly analysis of the 5dpf larvae, the interpupillary distance (IPD) and the head size defined by the otic vesicle and the semicircle of eyes as posterior and lower boundary were quantified using Image J software.[58]

Immunohistochemistry of zebrafish embryos

The control and morphant embryos at the 256-cell stage were fixed in 4% PFA/PBS at 4^0C overnight, followed by methanol fixation. The methanol-fixed embryos were rehydrated with 50% MeOH/PBS followed by PBS washes and then blocked in 1% BSA/PBST (1X PBS and 0.1% Triton X-100) for 2 hours at room temperature. The embryos were then incubated with primary antibody, prepared in blocking solution overnight at 4 °C. PBST washes were given followed by incubation with appropriate secondary antibody overnight at 4 °C. The embryos were again washed with PBST, and DAPI (1µg/ml) was added for 10min, washed with 1X PBS, and stored at -20 °C until imaging. For micronuclei analysis, the single cells were first labelled with ActinRed (1:200, Invitrogen R37112) for 14 hours at 4 °C, prior to DAPI staining. The image acquisition was done using Leica TCS SP8 confocal microscope and Zeiss ELYRA7 with Lattice SIM2 Super Resolution Microscope. The mitotic phenotypes were quantified by 3D reconstruction of the confocal images using the IMARIS software. The primary and secondary antibodies used in this study are listed in Fig.S7.

Immunoprecipitation and protein pull-down assay

Dechorionated and deyolked 1 dpf wild-type embryos were lysed in immunoprecipitation (IP) buffer (150 mM NaCl, 10 mM Tris HCl, pH 7.5, 1 mM EDTA, pH 8.0, 0.2 mM sodium orthovanadate, 1% NP40 and 1X Protease inhibitor) and centrifuged at 12,000 rpm for 20 mins at 4°C. The lysate was precleared by incubation with 25 µL of Protein A/G magnetic beads (Invitrogen: 78609) that was prewashed thrice with TBST (10 mM Tris HCl, pH 7.4, 15 mM NaCl, 0.01% Tween 20) at 4°C for 1 hour. Primary antibody (Cep57 and IgG) was added to the precleared cell lysate and kept at 4°C for 14-16 hours. 100 µL prewashed Protein A/G magnetic beads were added to the cell lysate and incubated overnight at 4°C. Using a magnetic stand, the flowthrough was collected and the beads were washed with IP buffer. For eluting the bound proteins, 2X Laemmli buffer was added to the beads, vortexed vigorously, and heated at 95°C for 10 mins. The eluate was then separated from the beads using a magnetic stand.

Label-free quantification and proteome analysis

For comparing the changes in the total proteome upon gene knockdown, label-free quantification was done using mass spectrometry. Lysates of 24hpf control and *cep57* morphant embryos were prepared using RIPA buffer. 100ug of total protein of each sample was separated on 10% SDS-PAGE gel. The gel was stained using Coomassie blue and destained with acetic acid and methanol. The protein-loaded lane was excised from the gel and fragmented into multiple pieces. The gel pieces were then alternately washed with 50 mM ammonium bicarbonate and acetonitrile to clear off the Coomassie blue stain from the gel pieces. Further, the gel pieces were subjected to reduction reaction using 10mM dithiothreitol followed by alkylation using 55mM iodoacetamide. In-gel trypsin digestion was carried out at 37^0C for 16 hours. The peptides were extracted using an extraction buffer (5% formic acid, 30% acetonitrile) and desalted using C18 reversed phase material-bound Zip Tips. The peptides were analyzed using the Thermo Scientific Easy-nLC 1200 system coupled to Q-Exactive mass spectrometer (Thermo Scientific). The peptides were resolved on a Thermo Scientific PepMap RSLC C18, 3µm, 100 A, 75 µm x 15 cm column (ES900) using a 5% - 25% - 45% - 95% -95%-3% Solvent B gradient followed at 0.00, 35.00, 41.00, 46.00, 49.00, 53.00 and 60.00 minutes respectively, (Solvent A: 5% acetonitrile - 0.2% formic acid; Solvent B: 90% acetonitrile - 0.2% formic acid), in DDA mode (data dependent mode). The nLC eluent was sprayed into the QE with a spray voltage of 2.2Kv

(kilovolts). The mass spectrometer was operated in the positive ion mode, and the settings with MS1 scans ranged over 400 – 1650 m/z, with AGC target, $3e^6$, resolution 70000. MS2 scans ranged over 200-2000m/z and resolution 17500. The data was acquired with the following set parameters: normalised collision energy 30, topN 10 peptides with charge exclusion 1, 6-8 and >8. The data was analysed using the Proteome Discoverer 2.2 software (Thermo Scientific), and the proteins were identified by performing a search against the *Danio rerio* Uniprot database (UP000000437). SEQUEST HT algorithm was used along with other analysis parameters such as trypsin enzyme specificity, carbamidomethyl static modification, mass tolerance set to 10ppm, and fragmentation tolerance set to 0.02 Da. Normalization mode was used for the total peptide amount along with pairwise ratio-based calculation. The percolator algorithm was used to validate peptide spectral matches (PSM), and a q-value cutoff of 0.01 (1% global False Discovery Rate, FDR) was used for proteome mapping, fold change, and GO analysis. ID mapping was performed using Uniprot, and Gene Ontology (GO) term analysis was performed using ShinyGO 0.76.2.[59,60]. Proteins with FDR<0.01 were qualified for quantification with a fold change cutoff ratio (FC) of >2.0 or <0.5 set as the threshold to identify differentially expressed proteins.

Statistical analysis

Each experiment was repeated a minimum of three times independently. GraphPad Prism software was used for all statistical analyses. All the values are shown as mean with SEM unless specified. Data were analysed using an unpaired *t-test* for statistical significance. A *P* value less than 0.05 was considered statistically significant.

Data availability

The mass spectrometry proteomics data have been deposited to the ProteomeXchange Consortium via the PRIDE [1] partner repository with the dataset identifier PXD062612.[61]

CRediT authorship contribution statement

Conceptualization: MK, Methodology: SI and MK, Validation: SI and MK, Formal analysis: SI and MK, Investigation: SI, LPSM, AG and MK, Resources: MK, Data curation: LPSM, SI and

MK, Writing – original draft: SI and MK, Writing – review and editing: MK, Visualization: SI and MK, Supervision: MK, Project administration: MK, Funding acquisition: MK

Declaration of competing interest

The authors have no competing interests.

Acknowledgments

We thank Dr. Santosh K. Guru, NIPER Hyderabad, for the Rb antibody and Dr. Indumathi Mariappan, BRIC inSTEM, Bangalore, for the Rb mutant zebrafish lines. We sincerely thank Mr. G. Srinivas, Advanced microscopy & Cell Sorting Facility, and Mr. B. Raman, Ms. Y. Kameshwari, and Mr. K. Ranjith Kumar, Proteomics Facility, CSIR-CCMB, for their technical assistance with the experiments. SI acknowledges CSIR, India, for the research fellowship. MK thanks the Anusandhan National Research Foundation (ANRF), Govt. of India (ANRF/ECRG/2024/000070/LS) and Council of Scientific and Industrial Research - Centre for Cellular and Molecular Biology (CSIR-CCMB), Govt. of India, for supporting and funding this research.

References:

1. De la Torre-García, O. *et al.* A homozygous CEP57 c.915_925dupCAATGTTCAGC mutation in a patient with mosaic variegated aneuploidy syndrome with rhizomelic shortening in the upper and lower limbs and a narrow thorax. *Eur. J. Med. Genet.* **62**, 195–197 (2019).

2. Watanabe, K., Takao, D., Ito, K. K., Takahashi, M. & Kitagawa, D. The Cep57-pericentrin module organizes PCM expansion and centriole engagement. *Nat. Commun.* **10**, (2019).

3. Ito, K. K. *et al.* Cep57 and Cep57L1 maintain centriole engagement in interphase to ensure centriole duplication cycle. *J. Cell Biol.* **220**, (2021).

4. Aziz, K. *et al.* Mosaic-variegated aneuploidy syndrome mutation or haploinsufficiency in Cep57 impairs tumor suppression. *J. Clin. Invest.* **128**, 3517–3534 (2018).

5. Zhao, H. *et al.* Cep57 and Cep57l1 function redundantly to recruit the Cep63-Cep152 complex for centriole biogenesis. *J. Cell Sci.* **133**, (2020).

6. Lukinavičius, G. *et al.* Selective chemical crosslinking reveals a Cep57-Cep63-Cep152 centrosomal complex. *Curr. Biol.* **23**, 265–270 (2013).

7. Emanuele, M. J. & Stukenberg, P. T. Xenopus Cep57 Is a Novel Kinetochore Component Involved in Microtubule Attachment. *Cell* **130**, 893–905 (2007).

8. Snape, K. *et al.* Mutations in CEP57 cause mosaic variegated aneuploidy syndrome. *Nat. Genet.* **43**, 527–529 (2011).

9. Sukla, S. *et al.* Crystal structure of human Cep57 C-terminal domain reveals the presence of leucine zipper and the potential microtubule binding region. *Proteins Struct. Funct. Bioinforma.* **92**, 1137–1143 (2024).

10. Wu, Q. *et al.* Cep57, a NEDD1-binding pericentriolar material component, is essential for spindle pole integrity. *Cell Res.* **22**, 1390–1401 (2012).

11. Zhou, H., Wang, T., Zheng, T., Teng, J. & Chen, J. Cep57 is a Mis12-interacting kinetochore protein involved in kinetochore targeting of Mad1-Mad2. *Nat. Commun.* **7**, 1–13 (2016).

12. He, R. *et al.* Cep57 protein is required for cytokinesis by facilitating central spindle microtubule organization. *J. Biol. Chem.* **288**, 14384–14390 (2013).

13. Langeh, N. *et al.* Mosaic variegated aneuploidy syndrome 2 with biallelic novel CEP57 splice site variation in Indian siblings: Expanding the clinical and molecular spectrum. *Clin. Genet.* **103**, 478–483 (2023).

14. Feng, B. *et al.* A novel CEP57 variant associated with mosaic variegated aneuploidy syndrome in a Chinese female presenting with short stature, microcephaly, brachydactyly, and small teeth. *Mol. Genet. Genomic Med.* **10**, 1–7 (2022).

15. Santos-Simarro, F. *et al.* Mosaic Variegated Aneuploidy syndrome 2 caused by biallelic variants in CEP57, two new cases and review of the phenotype. *Eur. J. Med. Genet.* **64**, 1–

7 (2021).

16. Pinson, L. *et al.* CEP57 mutation in a girl with mosaic variegated aneuploidy syndrome. *Am. J. Med. Genet. Part A* **164**, 177–181 (2014).

17. Ribeiro, J. H. *et al.* DNA damage and repair: underlying mechanisms leading to microcephaly. *Front. Cell Dev. Biol.* **11**, 1–20 (2023).

18. Dutton, K. A. *et al.* ectomesenchymal neural crest fates . 1–8 (2001).

19. Honoré, S. M., Aybar, M. J. & Mayor, R. Sox10 is required for the early development of the prospective neural crest in Xenopus embryos. *Dev. Biol.* **260**, 79–96 (2003).

20. Iyer, S. *et al.* Exposure to Tetrabutylammonium Bromide Impairs Cranial Neural Crest Specification, Neurogenic Program, and Brain Morphogenesis. *ACS Chem. Neurosci.* **14**, 1785–1798 (2023).

21. Luo, R., An, M., Arduini, B. L. & Henion, P. D. Specific pan-neural crest expression of zebrafish crestin throughout embryonic development. *Dev. Dyn.* **220**, 169–174 (2001).

22. Gou, Y., Guo, J., Maulding, K. & Riley, B. B. Sox2 and Sox3 Cooperate To Regulate Otic/Epibranchial Placode Induction in Zebrafish. *Dev. Biol.* **435**, 84–95 (2018).

23. Germanà, A. *et al.* Developmental changes in the expression of Sox2 in the zebrafish brain. *Microsc. Res. Tech.* **74**, 347–354 (2011).

24. Schulte-Merker, S., Van Eeden, F. J. M., Halpern, M. E., Kimmel, C. B. & Nüsslein-Volhard, C. no tail (ntl) is the zebrafish homologue of the mouse T (Brachyury) gene. *Development* **120**, 1009–1015 (1994).

25. Ballabeni, A., Zamponi, R., Moore, J. K., Helin, K. & Kirschner, M. W. Geminin deploys multiple mechanisms to regulate Cdt1 before cell division thus ensuring the proper execution of DNA replication. *Proc. Natl. Acad. Sci. U. S. A.* **110**, 8–13 (2013).

26. McGarry, T. J. & Kirschner, M. W. Geminin, an inhibitor of DNA replication, is degraded during mitosis. *Cell* **93**, 1043–1053 (1998).

27. Luo, L. & Kessel, M. Geminin coordinates cell cycle and developmental control. *Cell Cycle* **3**, 709–712 (2004).

28. Dimaki, M. *et al.* Cell cycle-dependent subcellular translocation of the human DNA licensing inhibitor geminin. *J. Biol. Chem.* **288**, 23953–23963 (2013).

29. Massacci, G., Perfetto, L. & Sacco, F. The Cyclin-dependent kinase 1: more than a cell cycle regulator. *Br. J. Cancer* **129**, 1707–1716 (2023).

30. Goshima, G., Nédélec, F. & Vale, R. D. Mechanisms for focusing mitotic spindle poles by minus end-directed motor proteins. *J. Cell Biol.* **171**, 229–240 (2005).

31. Atienzar, F. A., Venier, P., Jha, A. N. & Depledge, M. H. Evaluation of the random amplified polymorphic DNA (RAPD) assay for the detection of DNA damage and mutations. *Mutat. Res. - Genet. Toxicol. Environ. Mutagen.* **521**, 151–163 (2002).

32. Zhiyi, R. & Haowen, Y. A method for genotoxicity detection using random amplified

polymorphism DNA with Danio rerio. *Ecotoxicol. Environ. Saf.* **58**, 96–103 (2004).

33. Idilli, A. I., Pazzi, C., Dal Pozzolo, F., Roccuzzo, M. & Mione, M. C. Rad21 haploinsufficiency prevents ALT-associated phenotypes in zebrafish brain tumors. *Genes (Basel).* **11**, 1–14 (2020).

34. Cheng, H., Zhang, N. & Pati, D. Cohesin subunit RAD21: From biology to disease. *Gene* **758**, 144966 (2020).

35. Engeland, K. Cell cycle regulation: p53-p21-RB signaling. *Cell Death Differ.* **29**, 946–960 (2022).

36. Indovina, P., Pentimalli, F., Casini, N., Vocca, I. & Giordano, A. RB1 dual role in proliferation and apoptosis: Cell fate control and implications for cancer therapy. *Oncotarget* **6**, 17873–17890 (2015).

37. Pratama, E. *et al.* Critical role of ARID3B in the expression of pro-apoptotic p53-target genes and apoptosis. *Biochem. Biophys. Res. Commun.* **468**, 248–254 (2015).

38. Daddali, R., Ojaniemi, M., Hallman, M., Rämet, M. & Haapalainen, A. M. CPPED1-targeting microRNA-371a-5p expression in human placenta associates with spontaneous delivery. *PLoS One* **15**, 1–21 (2020).

39. Garcia, A. *et al.* Serine/threonine protein phosphatases PP1 and PP2A are key players in apoptosis. *Biochimie* **85**, 721–726 (2003).

40. Singh, P., Ravanan, P. & Talwar, P. Death associated protein kinase 1 (DAPK1): A regulator of apoptosis and autophagy. *Front. Mol. Neurosci.* **9**, 1–11 (2016).

41. Wang, S. *et al.* DAPK1 Signaling Pathways in Stroke: from Mechanisms to Therapies. *Mol. Neurobiol.* **54**, 4716–4722 (2017).

42. Zhang, T., Kim, B. M. & Lee, T. H. Death-associated protein kinase 1 as a therapeutic target for Alzheimer's disease. *Transl. Neurodegener.* **13**, 1–26 (2024).

43. Hermeking, H. & Benzinger, A. 14-3-3 Proteins in Cell Cycle Regulation. *Semin. Cancer Biol.* **16**, 183–192 (2006).

44. Pennington, K., Chan, T., Torres, M. & Andersen, J. The dynamic and stress-adaptive signaling hub of 14-3-3: emerging mechanisms of regulation and context-dependent protein–protein interactions. *Oncogene* **37**, 5587–5604 (2018).

45. Mayer, M. L., Gygi, S. P., Aebersold, R. & Hieter, P. Identification of RFC(Ctf18p, Ctf8p, Dcc1p): An alternative RFC complex required for sister chromatid cohesion in S. cerevisiae. *Mol. Cell* **7**, 959–970 (2001).

46. Bermudez, V. P. *et al.* The alternative Ctf18-Dcc1-Ctf8-replication factor C complex required for sister chromatid cohesion loads proliferating cell nuclear antigen onto DNA. *Proc. Natl. Acad. Sci. U. S. A.* **100**, 10237–10242 (2003).

47. Thadani, R., Kamenz, J., Heeger, S., Muñoz, S. & Uhlmann, F. Cell-Cycle Regulation of Dynamic Chromosome Association of the Condensin Complex. *Cell Rep.* **23**, 2308–2317 (2018).

48. Chen, E. S., Sutani, T. & Yanagida, M. Cti1/C1D interacts with condensin SMC hinge and supports the DNA repair function of condensin. *Proc. Natl. Acad. Sci. U. S. A.* **101**, 8078–8083 (2004).

49. Griese, J. J., Witte, G. & Hopfner, K. P. Structure and DNA binding activity of the mouse condensin hinge domain highlight common and diverse features of SMC proteins. *Nucleic Acids Res.* **38**, 3454–3465 (2010).

50. Belew, M. D., Chen, J. & Cheng, Z. Emerging roles of cyclin-dependent kinase 7 in health and diseases. *Trends Mol. Med.* **31**, 138–151 (2024).

51. Olson, C. M. *et al.* Development of a Selective CDK7 Covalent Inhibitor Reveals Predominant Cell-Cycle Phenotype. *Cell Chem. Biol.* **26**, 792-803.e10 (2019).

52. Park, S. Y., Kim, K. Y., Jun, D. Y., Hwang, S. K. & Kim, Y. H. G1 cell cycle arrest and extrinsic apoptotic mechanisms underlying the anti-leukemic activity of cdk7 inhibitor bs-181. *Cancers (Basel).* **12**, 1–22 (2020).

53. Pellarin, I. *et al.* Cyclin-dependent protein kinases and cell cycle regulation in biology and disease. *Signal Transduct. Target. Ther.* **10**, 11 (2025).

54. Journiac, N. *et al.* Cell Metabolic Alterations due to Mcph1 Mutation in Microcephaly. *Cell Rep.* **31**, (2020).

55. Kimmel, C. B., Ballard, W. W., Kimmel, S. R., Ullmann, B. & Schilling, T. F. Stages of embryonic development of the zebrafish. *Dev. Dyn.* **203**, 253–310 (1995).

56. Suzuki, K., Bose, P., Leong-Quong, R. Y., Fujita, D. J. & Riabowol, K. REAP: A two minute cell fractionation method. *BMC Res. Notes* **3**, 294 (2010).

57. Shepard, J. L., Stern, H. M., Pfaff, K. L. & Amatruda, J. F. Analysis of the cell cycle in zebrafish embryos. *Methods Cell Biol.* **2004**, 109–125 (2004).

58. Faundes, V. *et al.* Impaired eIF5A function causes a Mendelian disorder that is partially rescued in model systems by spermidine. *Nat. Commun.* **12**, 1–13 (2021).

59. Ge, S. X., Jung, D., Jung, D. & Yao, R. ShinyGO: A graphical gene-set enrichment tool for animals and plants. *Bioinformatics* **36**, 2628–2629 (2020).

60. Deracinois, B., Flahaut, C., Duban-Deweer, S. & Karamanos, Y. Comparative and quantitative global proteomics approaches: An overview. *Proteomes* **1**, 180–218 (2013).

61. Perez-Riverol, Y. *et al.* The PRIDE database at 20 years: 2025 update. *Nucleic Acids Res.* **53**, D543–D553 (2025).

Legends:

Figure 1: Cep57 localizes to centrosomes and is essential for early neurodevelopment

A: Sum projection confocal images of 256 cell stage WT embryos showing centrosomal staining by γ tubulin (red), Cep57 (green, red asterisks), and DNA (blue/DAPI). Scale bars, 50µm. B: Western blot showing localization of Cep57 in whole embryonic lysate, nuclear and cytoplasmic fractions. Lamin B1 and Gapdh represents nuclear and cytoplasmic fractions respectively. C: Western blot showing Cep57 levels in control and morpholino-injected embryos. Gapdh was used as the loading control. D: Quantification showing percent phenotype of *cep57* splice morpholino injected, splice morpholino coinjected with *cep57* mRNA, and *cep57* mRNA only. Data are shown as mean ± SEM, *p<0.05, **p<0.01, ***p<0.001. n=3 for each experiment. E: Gross morphological analysis of *cep57*-depleted embryos in comparison to control at 10 somite and 24hpf stage, showing somite architecture anomalies (red asterisk), midbrain-hindbrain boundary (double red asterisk), and body axis defects (red arrow). Scale bars, 100µm for 10 somite and 50µm for 24hpf embryos. F: Whole mount skeletal preparations of 5dpf control and *cep57* morphant larvae showing cartilage and bone staining (red asterisk) using Alcian blue and Alizarin red S, respectively. Scale bars, 100µm. G: Quantification of microcephaly-associated features – interpupillary distance (IPD) and head area in control and *cep57* morphants. Data are shown as mean ± SEM, *p<0.05, **p<0.01, ***p<0.001. n=3 for each experiment.

Figure 2: Cep57 is essential for cell survival, genome stability and cell cycle progression

A: Whole-mount acridine orange staining to visualize apoptotic cells (red asterisks) in control and *cep57* morphants. Scale bar, 100µm. B: Whole-mount TUNEL staining in control and *cep57* morphants. Scale bar, 100µm. C, D: Fluorescence-based flow cytometry analysis in control and *cep57* morphants showing different phases of the cell cycle at 1dpf (C) and 2dpf (D). E, F: Quantification of cells in each phase of the cell cycle in control and cep57 morphants at 1dpf (E) and 2dpf (F). Data are shown as mean ± SEM, *p<0.05, **p<0.01, ***p<0.001. n=3 for each experiment.

Figure 3: Loss of Cep57 results in PCM disorganization, DNA damage, and supernumerary micronuclei

A: Western blot showing Geminin, Cdk1 and phospho Cdk1 levels in control and morpholino-injected embryos across developmental stages. Gapdh or Tubulin was used as the loading control. B, C: Sum projection confocal images of 256 cell stage control and *cep57* morphant embryos showing microtubule and centrosomal staining at metaphase (B) and interphase (C) by α tubulin (red), γ tubulin (green, red asterisks) respectively, and DNA (blue/DAPI). Scale bars, 50µm. D: Quantification of *cep57* morphant embryos showing spindle pole focusing defects. All data are shown as mean ± SEM. *p<0.05, **p<0.01, ***p<0.001. n=3 for each experiment. E: Sum projection SIM^2 images of 256 cell stage control and *cep57* morphants showing centrosomal staining γ tubulin (red), centrioles (green) and DNA (blue/ DAPI). Scale bars, 10µm. F: Sum projection SIM^2 images of cells from control and *cep57* morphants showing cell membrane (actin red) and DNA (blue/ DAPI) at bud stage and 24hpf. Scale bars, 2µm.

Figure 4: Cep57 interacts with Geminin to regulate Rb1-mediated G1/S transition

A: Comet assay to estimate DNA damage in control and *cep57* morphants. All data are shown as mean ± SEM. *p<0.05, **p<0.01, ***p<0.001. n=3 for each experiment. B: Western blot showing Rad21 levels in control and morpholino-injected embryos. Gapdh was used as the loading control. C: Immunoblot showing Rad21 as an interactor of Cep57 in endogenous immunoprecipitation assay. D: Quantitative real-time PCR plots showing relative transcript levels of *p53* and *p21*. All data are shown as mean ± SEM. *p<0.05, **p<0.01, ***p<0.001. n=3 for each experiment. E: Western blot showing Rb and phospho Rb levels in control and morpholino-injected embryos. Gapdh was used as the loading control. F: Quantification of Fluorescence-based flow cytometry analysis in control and *cep57* morphants showing different phases of the cell cycle in control, cep57 knockdown and Rb mutant background. Rb mutant background served as positive control. All data are shown as mean ± SEM. *p<0.05, **p<0.01, ***p<0.001. n=3 for each experiment. G: Western blot showing Geminin levels in control, *cep57* morphants and *cep57* depletion in Rb mutant background. Gapdh was used as the loading control. H: Immunoblot showing Geminin as an interactor of Cep57 in endogenous immunoprecipitation assay. I: Western blot showing Geminin levels in control, *cep57*-depleted

embryos, and *cep57* depleted embryos injected with Cep57 mRNA. Gapdh was used as the loading control.

Figure 5: Cep57 regulates cell cycle modulators and DNA damage-inducing proteins

A: Volcano plot showing fold change in differentially expressed proteins in control vs *cep57* morphants. B: Quantitative real-time PCR plots showing relative transcript levels of *smc4, ctf8, dapk1* and *arid3b* in control and *cep57* morphants. All data are shown as mean ± SEM. *p<0.05, **p<0.01, ***p<0.001. n=3 for each experiment. C: Schematic representation showing *cep57* function in genome stability, faithful chromosome segregation, cell cycle progression, and early neurodevelopment.

Figure S1:

A: Sum projection confocal images of 256 cell stage WT embryos showing centrosomal staining by γ tubulin (red), nuclear staining of Cep57 (green, white asterisks), and DNA (blue/DAPI). Scale bars, 50µm. B: RT-PCR analysis of *cep57* transcripts in different developmental stages. β-actin was used as the loading control. C: Western blot showing Cep57 levels in different developmental stages till 24hpf. Gapdh was used as the loading control. D: Whole-mount RNA *in situ* hybridization showing *cep57* expression during early development. Scale bars,100µm.

Figure S2:

A: Quantification showing percent phenotype of control and *cep57* morphants injected with 1mM *cep57* translation blocker morpholino. Data are shown as mean ± SEM, *p<0.05, **p<0.01, ***p<0.001. n=3 for each experiment. B: Quantification showing percent phenotype of control and *cep57* morphants injected with 0.1mM and 0.5mM *cep57* translation blocker morpholinos. Data are shown as mean ± SEM, *p<0.05, **p<0.01, ***p<0.001. n=3 for each experiment. C: PCR-based validation of intron retention in *cep57* morphants injected with splice morpholino and rescue of splicing event when coinjected with *in vitro* transcribed cep57mRNA. mRNA alone-injected embryos showed correct splicing. No template control (NTC) was used as a negative control. D: Gross morphological analysis of *cep57* morphants P0, P1, P2, and P3 at different stages of larval development.

Figure S3:

Quantitative real-time PCR plots showing relative transcript levels of microcephaly markers *mcph1*, *wdr62*, *ankle2*, *map11*, *kif14*, and *aspm*. All data are shown as mean ± SEM. *p<0.05, **p<0.01, ***p<0.001. n=3 for each experiment.

Figure S4:

Spatiotemporal gene expression analysis by *in situ* hybridization in control and *cep57* morphants at 6 somite and 24hpf stage. A, B, C: *Crestin*, *snail2*, and *sox10* expression in the 6 somite control and *cep57* (red asterisk) morphants. D, E, F: *Crestin*, *snail2*, and *sox10* expression in 24hpf control and *cep57* (double red asterisk) morphants. G: *Sox2* expression in 24hpf control and *cep57* (red asterisk) morphants. Scale bars, 100µm. H: *Tbxta* expression in 24hpf control and *cep57* (red arrow) morphants. Scale bar, 50µm.

Figure S5:

A: PCR-based RAPD assay showing polymorphic bands (red arrows) in control and *cep57* morphants. B: Quantification of RAPD assay to estimate genomic instability in control and *cep57* morphants. All data are shown as mean ± SEM. *p<0.05, **p<0.01, ***p<0.001. n=3 for each experiment. C: Sum projection confocal images of 256 cell stage control and *cep57* morphant embryos showing mitotic cells by PH3 (green) and DNA (blue/DAPI). Scale bars, 50µm. D: Western blot showing Cyclin E levels in in control and *cep57* morphants. Gapdh was used as the loading control.

Figure S6:

GO analysis of all the upregulated and downregulated proteins in *cep57* morphants, respectively.

Figure S7:

List of all the antibodies used in this study.

Figure S8:

List of all the primers used in this study.

Figure S9:

List of all differentially expressed protein from LC-MS/MS analysis.

Figure 1

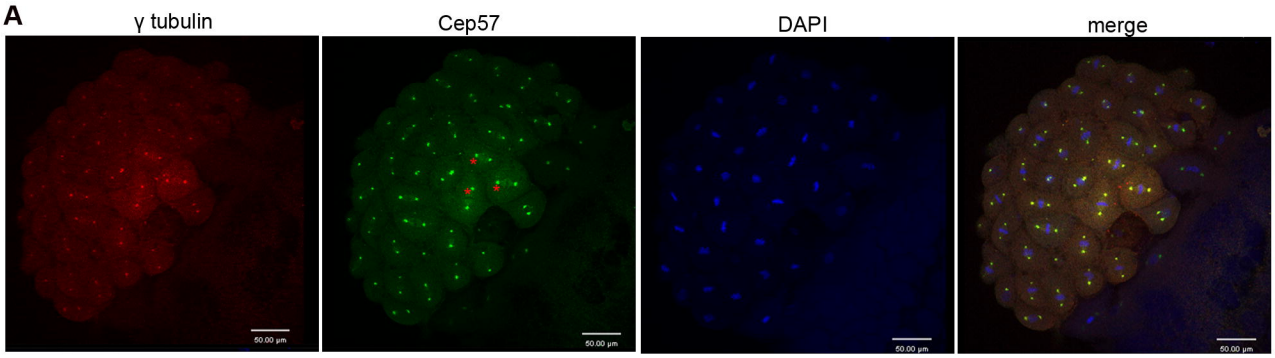
A
γ tubulin
Cep57
DAPI
merge

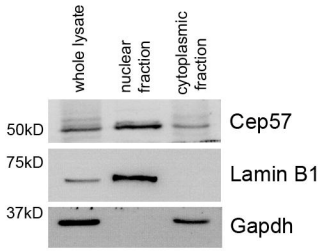
B
whole lysate
nuclear fraction
cytoplasmic fraction
50kD
Cep57
75kD
Lamin B1
37kD
Gapdh

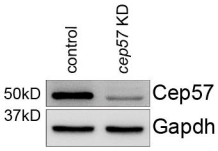
C
control
cep57 KD
50kD
Cep57
37kD
Gapdh

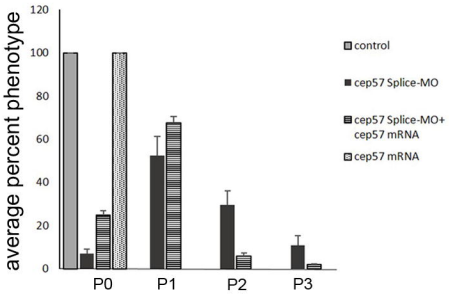
D
average percent phenotype
120
100
80
60
40
20
0
P0
P1
P2
P3
control
cep57 Splice-MO
cep57 Splice-MO+ cep57 mRNA
cep57 mRNA

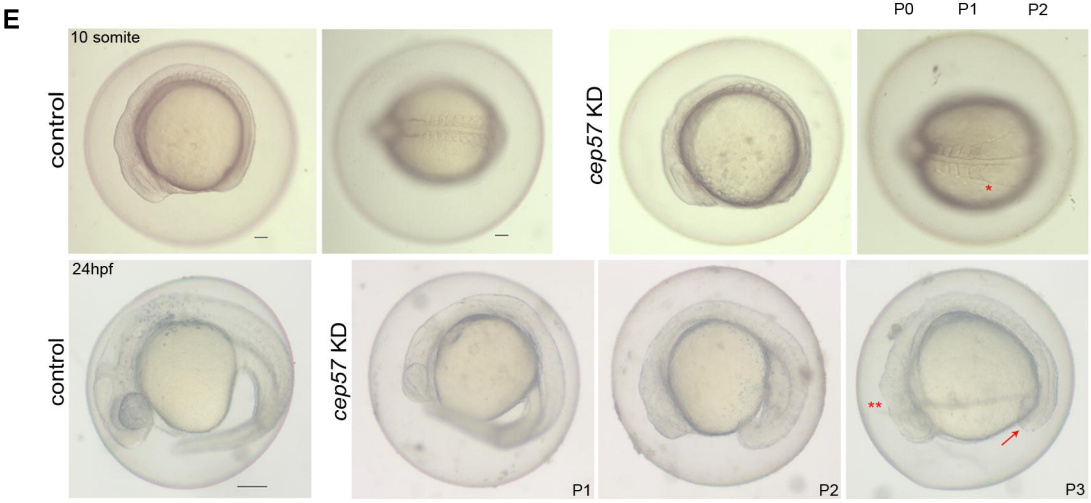
E
10 somite
control
cep57 KD
24hpf
control
cep57 KD
P1
P2
P3

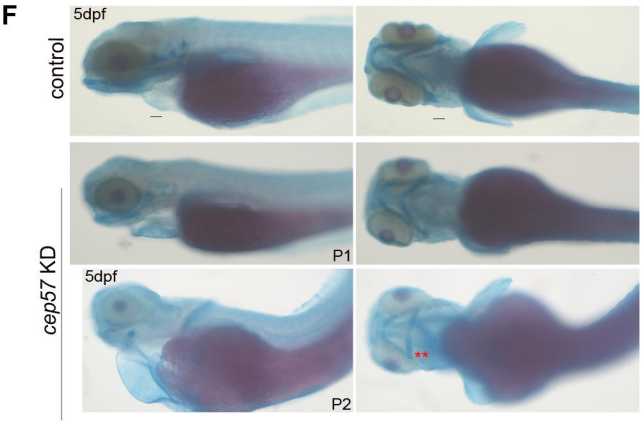
F
5dpf
control
cep57 KD
P1
5dpf
P2

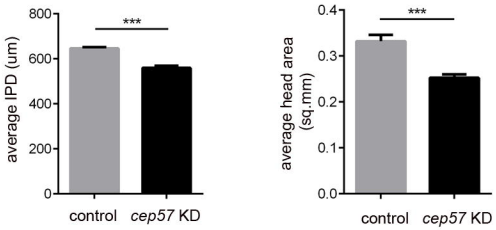
G
average IPD (um)
800
600
400
200
0
***
control
cep57 KD
average head area (sq.mm)
0.4
0.3
0.2
0.1
0.0
***
control
cep57 KD

Figure 2

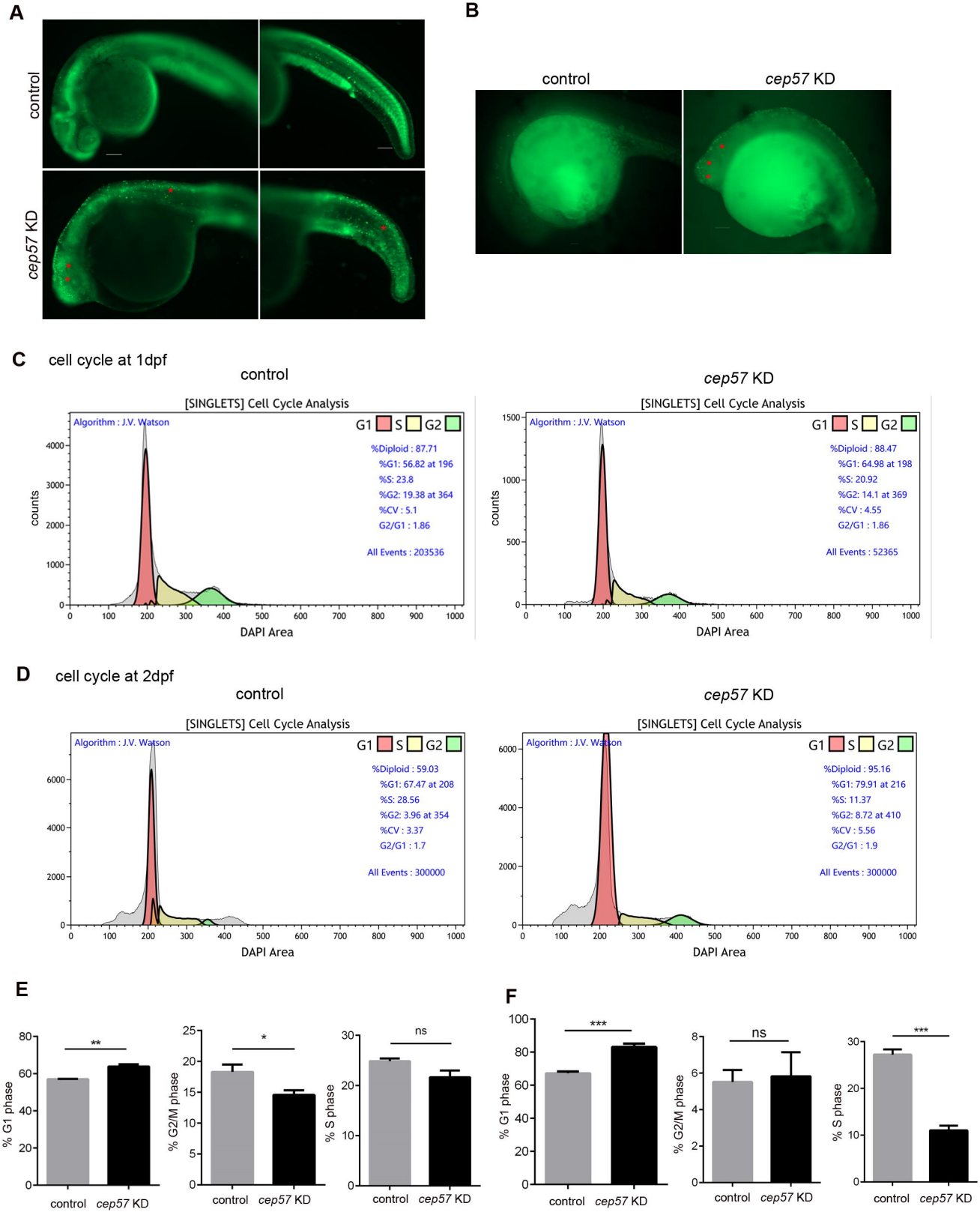
A
control
cep57 KD
B
control
cep57 KD
C
cell cycle at 1dpf
control
[SINGLETS] Cell Cycle Analysis
Algorithm : J.V. Watson
G1 S G2
%Diploid : 87.71
%G1: 56.82 at 196
%S: 23.8
%G2: 19.38 at 364
%CV : 5.1
G2/G1 : 1.86
All Events : 203536
counts
DAPI Area
cep57 KD
[SINGLETS] Cell Cycle Analysis
Algorithm : J.V. Watson
G1 S G2
%Diploid : 88.47
%G1: 64.98 at 198
%S: 20.92
%G2: 14.1 at 369
%CV : 4.55
G2/G1 : 1.86
All Events : 52365
counts
DAPI Area
D
cell cycle at 2dpf
control
[SINGLETS] Cell Cycle Analysis
Algorithm : J.V. Watson
G1 S G2
%Diploid : 59.03
%G1: 67.47 at 208
%S: 28.56
%G2: 3.96 at 354
%CV : 3.37
G2/G1 : 1.7
All Events : 300000
DAPI Area
cep57 KD
[SINGLETS] Cell Cycle Analysis
Algorithm : J.V. Watson
G1 S G2
%Diploid : 95.16
%G1: 79.91 at 216
%S: 11.37
%G2: 8.72 at 410
%CV : 5.56
G2/G1 : 1.9
All Events : 300000
DAPI Area
E
% G1 phase
**
control
cep57 KD
% G2/M phase
*
control
cep57 KD
% S phase
ns
control
cep57 KD
F
% G1 phase
***
control
cep57 KD
% G2/M phase
ns
control
cep57 KD
% S phase
***
control
cep57 KD

Figure 3

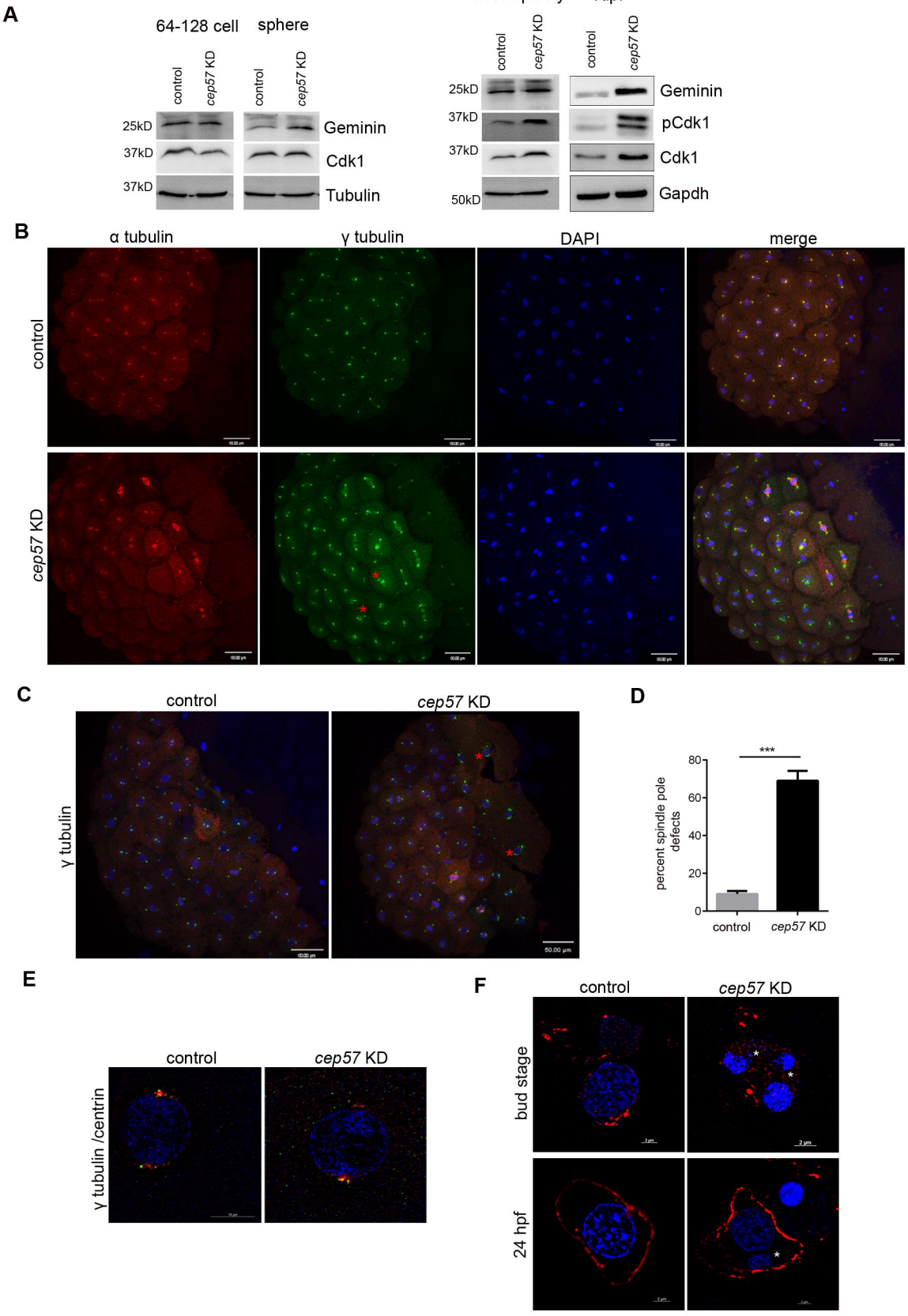
A
64-128 cell
sphere
control
cep57 KD
control
cep57 KD
25kD
37kD
37kD
Geminin
Cdk1
Tubulin
50% epiboly
1dpf
control
cep57 KD
control
cep57 KD
25kD
37kD
37kD
50kD
Geminin
pCdk1
Cdk1
Gapdh
B
α tubulin
γ tubulin
DAPI
merge
control
cep57 KD
C
control
cep57 KD
γ tubulin
D
***
percent spindle pole defects
80
60
40
20
0
control
cep57 KD
E
control
cep57 KD
γ tubulin /centrin
F
control
cep57 KD
bud stage
24 hpf

Figure 4

A

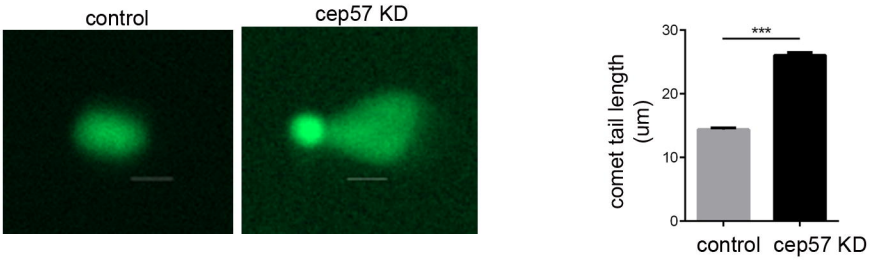

B

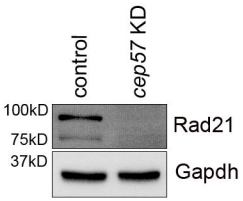

C

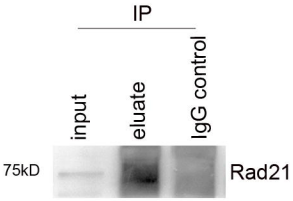

D

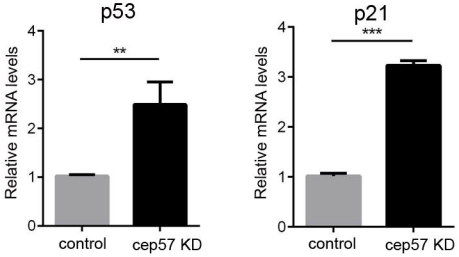

E

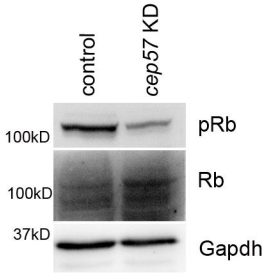

F

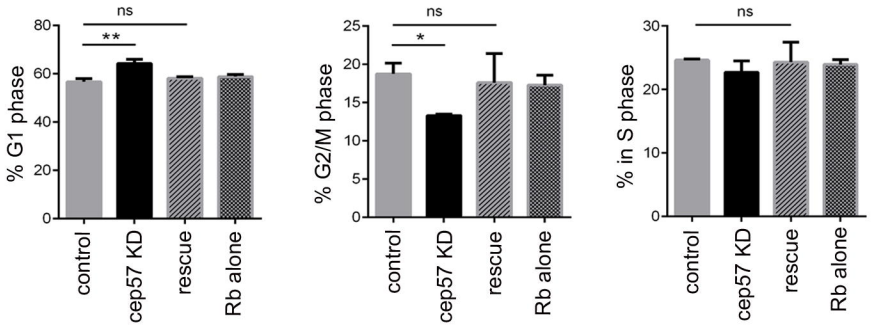

G

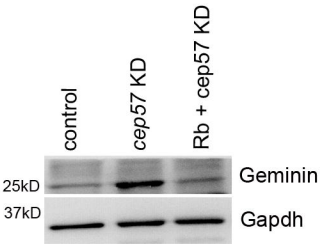

H

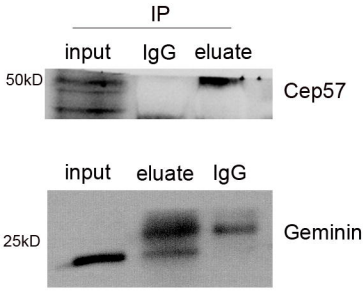

I

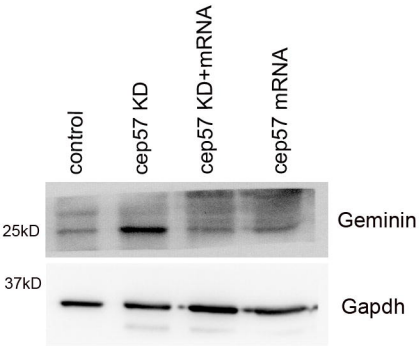

Figure 5

A

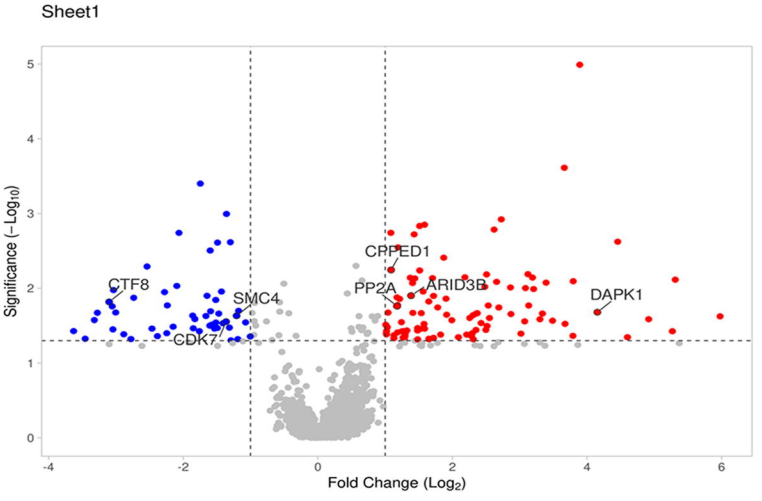
Sheet1
Significance (−Log10)
Fold Change (Log2)
CTF8
SMC4
CDK7
CPPED1
PP2A
ARID3B
DAPK1

B

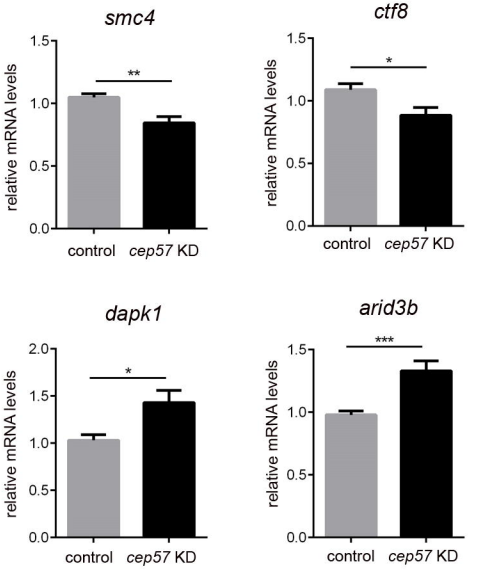
smc4
ctf8
dapk1
arid3b
relative mRNA levels
control
cep57 KD

C

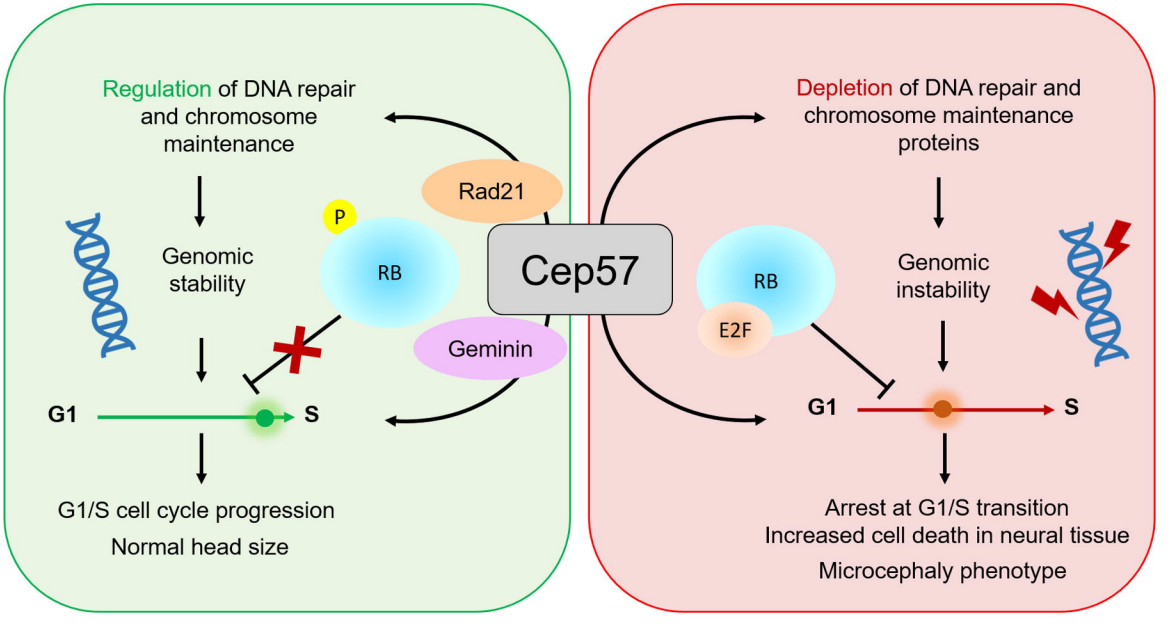
Regulation of DNA repair and chromosome maintenance
Genomic stability
G1
S
G1/S cell cycle progression
Normal head size
P
RB
Rad21
Geminin
Cep57
Depletion of DNA repair and chromosome maintenance proteins
Genomic instability
RB
E2F
G1
S
Arrest at G1/S transition
Increased cell death in neural tissue
Microcephaly phenotype